Article

N-Doped and Sulfonated Reduced Graphene Oxide Supported PtNi Nanoparticles as Highly Efficient Electrocatalysts for Oxygen Reduction Reaction

Chun Ouyang [1], Damao Xun [2,*] and Gang Jian [1]

[1] School of Material Science and Engineering, Jiangsu University of Science and Technology, Zhenjiang 212003, China; oyc1014@just.edu.cn (C.O.); gjian@just.edu.cn (G.J.)

[2] College of Communication and Electronics, Jiangxi Science and Technology Normal University, Nanchang 330038, China

* Correspondence: damao65@163.com

Abstract: N-doping and sulfonation is prepared on the reduced graphene oxide (rGO) support for PtNi nanoparticles (PtNi/S-(N)rGO) by a simple method of hydrothermal synthesis and thermal decomposition. The specific surface area increases from 180.7 m^2/g of PtNi/rGo to 293.5 m^2/g of PtNi/S-(N)rGO. The surface morphology shows wrinkles sites, which are separated by the sulfonated groups. The catalytic stability and efficiency are improved by the anchoring effect of sulfonated groups and evenly distribution of nanoparticles, respectively. The synergistic effect of N-doping and sulfonation can be in favor of catalytic efficiency by the increase of number of electron transfer. The half-wave potential of the PtNi/S-(N)rGO catalyst is up to 0.632 V, a small positive shift compared to the Pt/C catalyst. The durability of the PtNi/S-(N)rGO is 2.6 times higher than of the Pt/C catalyst after 5000 repeated cycles. The peak power of the PtNi/S-(N)rGO catalyst increased 37.5% compared to the Pt/C catalyst. Therefore, the stability and catalytic efficiency are improved by the PtNi/S-(N)rGO catalyst applied in proton exchange membrane fuel cell (PEMFC) compared to the commercial Pt/C catalyst.

Keywords: electrocatalysis; nitrogen-doping; sulfonation; oxygen reduction reaction; proton-exchange membrane fuel cell

1. Introduction

The half-reaction of ORR was sluggish kinetics in the whole process of redox reaction. Adequate materials need to be developed to catalyze such reaction efficiently. The catalytic efficiency of ORR was still lower than that of counter anodic part of hydrogen oxidation reaction after considerable efforts done by researchers. The catalysts of commercial use are platinum materials [1]. Pt-base catalysts were efficient to improve the oxygen reduction reaction (ORR) in proton exchange membrane fuel cells (PEMFCs) [2]. The precious scarcity and stability of Pt were the key points to restrict the large-scale commercial applications in vehicle and portable devices [3]. The efforts were focused on minimizing usage of Pt, Pt-free metal catalyst, and supporting materials for reducing the cost and improving the stability of catalysts.

The bimetallic catalysts were seriously considered with different metal elements such as PtNi [4], PtCo [5], PtPd [6], PtFe [7], PtAg [8], PtRu [9], etc. Among these catalysts, PtNi alloys were discussed mostly as a catalyst to reduce the usage of Pt. PtNi porous films were prepared with active sites for improving the ORR. The species of PtNi surfaces were adsorbed by the oxygen-containing functional groups. Then, more Pt(111) facets were formed, which showed better ORR activity with low Pt loading [10]. PtNi nanoparticles with 10 nm were embedded into the carbon layer. The mass activity and specific activity were shown 6.5 and 8.4 times compared to the commercial Pt/C catalyst [11], respectively.

The surface of PtNi nanoparticles were introduced Cu element, which can improve the stability of PtNi catalysts [12]. Pd nanowires were selected as medium to improve the epitaxial of Pt and Ni. With introduction of Pd core, the high index exposed facets of PtNi alloy were formed. It was very useful for catalytic performance [13]. Martins et al. provided the PtNi nanoparticles on the binary metal oxide (BMO) supports. The metal oxide lowered the activation energies for ORR. Moreover, the PtNi/BMO catalysts could lower the cost and strength [14]. The two-dimension graphene was shown best conductivity and super specific surface area [15]. Therefore, the graphene was used as support materials for ORR in the PEMFCs because of good physical properties. By introducing heteroatom and grafting group on graphene, the stability and catalytic efficiency were improved greatly than that of the commercial Pt/C catalysts.

The doping element could significantly affect the properties of ORR. The charge distribution, structure, band gap, and composition of catalysts were adjusted with different formation of doping to obtain the activated sites. The graphitic and pyridinic N could promote the adsorption and activation of species [16]. The OOH* groups from the protonated O_2 preferred to bind with C atom at the adjacent with graphite N. The charges of graphene were redistributed to lower the activation energy of reaction of O_2 [17]. The P element was VA group, similar with nitrogen [18]. The P atom was incorporated into the carbon sheet and oxidized partly. The activated sites appeared for ORR at the doped places [19]. The graphite oxide and triphenylphosphine was used to prepare P-doped graphene by simple and low-cost method. The catalytic activity and stability were greatly improved [20]. The graphene supports were potential to apply in the metal-free catalyst. The graphene doped by N and P were used to improve the catalytic efficiency and stability by two simple steps [21]. Furthermore, the N, P, and F doped graphene were prepared by thermal activation. These catalysts were shown the excellent electroactivities for ORR [22]. C-S covalent bonds were in favor of improving the kinetics of reaction and stability as supports of the catalysts. Among the ORR, the current density of the cathodes were higher to 25.66 mA cm^{-2} at 0.89 V (vs. RHE) [23]. In the process of operation for PEMFCs, the key step was decided by the oxygen reduction reaction (ORR). In the process of electron transfer, the complex species and pathway caused the breakage of O-O band more difficultly, which make the sluggish kinetic of ORR [24]. In order to solve such problems, catalysts and supports were needed to facilitate the transmission of reactant and lower the activation energy [25]. The support materials were not only as the carrier but also affect the process of ORR while interacting with catalysts [26]. Sulfonic acid group was in favor of hydrophobic of Pt-loading. The structure and surface properties were changed by sulfonation, which could lower the size of particles and improve the distribution evenly. The catalytic efficiency was greatly improved by sulfonated graphene nanosheet-supported platinum [27]. The oxidized sulfur was grafted on the metal-free electrocatalysts for ORR from cassava residues. The best activities of sulfur functionalized on cassava residues was from the carbonization of 800 °C which was caused by the four electron pathways, which was different from the two electron pathway at carbonization of low temperature [28]. The remarkable stability of N-doped ordered mesoporous carbon hollow spheres electrocatalysts from nitrogen sources of 2-pyridinecarboxaldehyde was attributed to the modification of N-quaternary to N-pyridinic species, while the N-pyrrolic species oxidized to N-quaternary with the nitrogen sources of N-pyrrole after accelerated degradation test [29]. Carbon materials were corroded in the acid environment with high anodic potential after operation of PEMFCs. The electrochemical stability was greatly improved by the higher graphitic nature from in-situ grown N-doped graphene shell [30].

This work aimed at the doping and sulfonation on graphene with PtNi nanoparticles as the catalyst. The character of catalyst for ORR was investigated by the rotating disk electrode (RDE) in the 0.5 mol/L H_2SO_4 electrolyte. The current density and power density were evaluated by the single cell of PEFMC. The catalyst with high catalytic efficient will begin the potential application in the PEMFCs.

2. Experimental

All chemical reagents were analytically pure (AR, 99%). The graphene oxide (GO) was purchased from XFNANO corporation. The urea was used as nitrogen sources. The 20 mL of 8 mg/mL graphene oxide solution and 2 g urea were dispersed in the 30 mL deionized water by ultra-sonification for 1 h. Then, the solution was poured into the Teflon-lined autoclave for 8 h under 180 °C. After cooling to room temperature, the samples were cleaned by deionized water three times to remove the residual. After drying by vacuum freeze-drying machine, the graphene oxide was reduced into graphene doped by N, which was denoted as (N)rGO. $(NH_4)_2SO_4$ and (N)rGO were mixed with the weight ratio of 1:4 in the deionized water for uniform mixing. Then, the solutions were dried under reduced pressure in a rotary evaporator. Next, the powder of (N)rGO and $(NH_4)_2SO_4$ were placed into the quartz tube furnace under following Ar gas at 230 °C, while the -SO_3H groups were grafted on the (N)rGO to form sulfonated groups denoted as S-(N)rGO by the decomposition of $(NH_4)_2SO_4$. $H_2PtCl_6 \cdot H_2O$ and $Ni_2SO_4 \cdot 6H_2O$ were mixed with the weight ratio of 1:1. S-(N)rGO was added into the precursor of Pt and Ni under ultra-sonification for 30 min. The ethylene glycol (200 mL) was added into the above suspension (metal loading of 20 wt.%) under 150 °C with Ar atmosphere for 3 h. Then, the suspensions were cleaned and filtered with deionized water for several times. After drying, the samples of catalyst denoted as PtNi/S-(N)rGO were finished. The PtNi/S-rGO and PtNi/rGO samples were prepared by a similar way.

The phases of samples were analyzed by the X-ray diffraction (XRD, Bruke D8 Advance, Karlsruhe, Germany), which was under Cu Kα in the 2θ range from 10° to 80° with the scan rate of 2°/min. The structure and morphology of catalysts were characterized by the field scanning electron microscope (FE-SEM, Hitachi Regulus-8100, Tokyo, Japan) with EDX analysis and transmission electron microscope (TEM, JEOL JFM-2100F, Akishima, Japan). X-ray photoelectron (XPS) was used by ThermoFisher IS 50, Waltham, USA. Raman spectra of catalysts were recorded by the Bruker RAM II instrument (Karlsruhe, Germany) with a 520 nm-wavelength laser.

The ORR curves of the catalyst were conducted by the three electrode-systems using the linear sweep voltammetry and rotating circle-disk galssy carbon electrode (d = 3 mm). The Pt plate (S = 1 cm^2) and Hg/HgO electrode were used as counter and reference electrode, respectively. The catalysts were used as working electrode attached on the rotary system connected on the electrochemical workstation (Princeton Applied Research, Model 636A). The 15 mg catalyst was dispersed into an ethanol solution of 5 mL with 50 μL of 5 wt.% Nafion solution. After being mixed under ultra-sonification, the suspension including catalysts was prepared. The 20 μL of the suspension was coated on the glassy carbon electron. After evaporation of solvent at room temperature, the working electrode was finished. In order to saturate the solution, O_2 was bubbled into the solution within 30 min. During the process of the electrochemical measurement, O_2 atmosphere was filled in the above solution in the process of measurement. The linear sweep voltammetry (LSV) was conducted in the 0.5 M (mol/L) H_2SO_4 solution at the rotation rate of 800 rpm. The scanning rate was 10 mV·s^{-1} with the potential range from 0 to 1.0 V (vs. RHE) at ambient temperature.

The durability of catalysts was conducted by the cyclic voltammetry (CV) between −0.1 and 1.0 V (vs. RHE) in 0.5 M H_2SO_4 electrolyte for 5000 cycles. After the test of durability, the CV curves were measured from −0.1 to 1.0 V (vs. RHE) at the scanning rate of 20 mV·s^{-1}. The electrochemical active surface area (ECSA) of Pt was conducted by the integrating desorption peak area of hydrogen as shown in Equation (1):

$$ECSA = S_H / (Q_{ref} \times v \times m) \tag{1}$$

where ECSA (cm^2/g) was the electrochemical specific surface area of Pt, S_H (A V/cm^2) was the area of hydrogen desorption, v (V/s) was scanning rate of CV, Q_{ref} was the electron

quantity from oxidation of a single-layer hydrogen atom on the smooth Pt surface, and *m* was the density of loading on the working electrode.

The cathodes of PEMFC measurement were Pt/C and PtNi/S-(N)rGO. The anode of PEMFC was prepared by mixing the 5.0 mg of 20 wt.% Pt/C catalyst, 100.0 μL of 5 wt.% Nafion solution, and 5 mL of ethanol under ultra-sonification for 5 min. The mixture was coated on the carbon paper of the diffusion layer. The area of carbon paper was 1.0 cm × 5.0 cm. The loading of carbon paper was 1 mg/cm^2.

The cathode was prepared with the similar method as the anode. The PtNi/S-(N)rGO and Pt/C were the catalysts, and the loading density was 1 mg/cm^2. The membrane electrode was prepared as follows. The Nafion XL membrane was hot pressed with both Pt/C and PtNi/S-(N)rGO electrodes at 10 MPa under 130 °C for 90 s. The measurement of single cell was prepared by the Yuke fuel cell test equipment (YukeInovation, YK-M10). The pressure of hydrogen and oxygen were set at 0.1 MPa, which was humidified (RH = 100%). The operation temperature of fuel cell was 70 °C.

3. Results and Discussion

XRD pattern of PtNi/S-(N)rGO was shown in Figure 1. The peaks around 39.7°, 46.2°, and 68.2° indicated Pt(111), Pt(200), and Pt(220) (JCPDS 04-0802), respectively. The broader peaks of Pt were caused by the PtNi metal alloys with the structure of solution. The amount of PtNi was formed. The face-centered cubic Pt crystal appeared. All of these peaks were coincided with results reported by [31]. The Pt and PtNi were simple synthesized by the chemical reduction while the graphene oxide was reduced into graphene at the same time. The C peak with a d-spacing of about 0.381 nm for PtNi/S-(N)rGO is shown in Figure 1, compared to a d-sapcing of about 0.343 nm of pristine graphite in the literature [27]. The activated sites by N doping also provided the binding of oxygen functional groups. The increase of d-sapcing was attributed to sulfonation groups and oxygen functional groups [32].
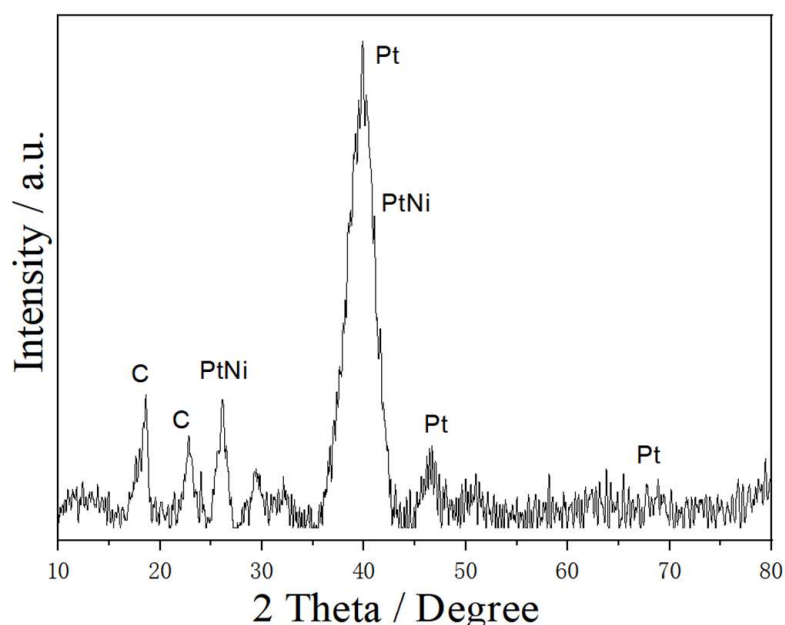

Figure 1. XRD patterns of PtNi/S-(N)rGO catalyst.

The SEM images of PtNi/S-(N)rGO were shown with morphology of the wrinkled layers in Figure 2a,b. The supported materials exhibited the wrinkles sites and sheets-like morphology. The similar molecular structure of oxygen functional groups on graphite surface were described in reference [32]. Figure 2c,d showed the FE-SEM images of GO and PtNi/S-(N)rGO catalyst, respectively. N element was doped into the graphene oxide by the hydrothermal method from urea as N source. The rGO was prepared by the reduction of GO.

The sulfonated groups were used to separate the rGO sheets and the nanoparticles of PtNi were anchored at the sulfonated groups on the rGO evenly in Figure 2d. It was indicated by the results of XRD in Figure 1. The whole flexible structure was not changed by the process of sulfonation and deposition of PtNi nanoparticles compared with Figure 2b–d. The element mapping was achieved to distinguish the N and S distribution on the graphene supports. As shown in Figure 2e,f, N and S elements had similar distribution, which demonstrated good N-doping and sulfonation in the graphene support material. The evenly distribution of S could strengthen the evenly distribution of anchored PtNi nanoparticles.
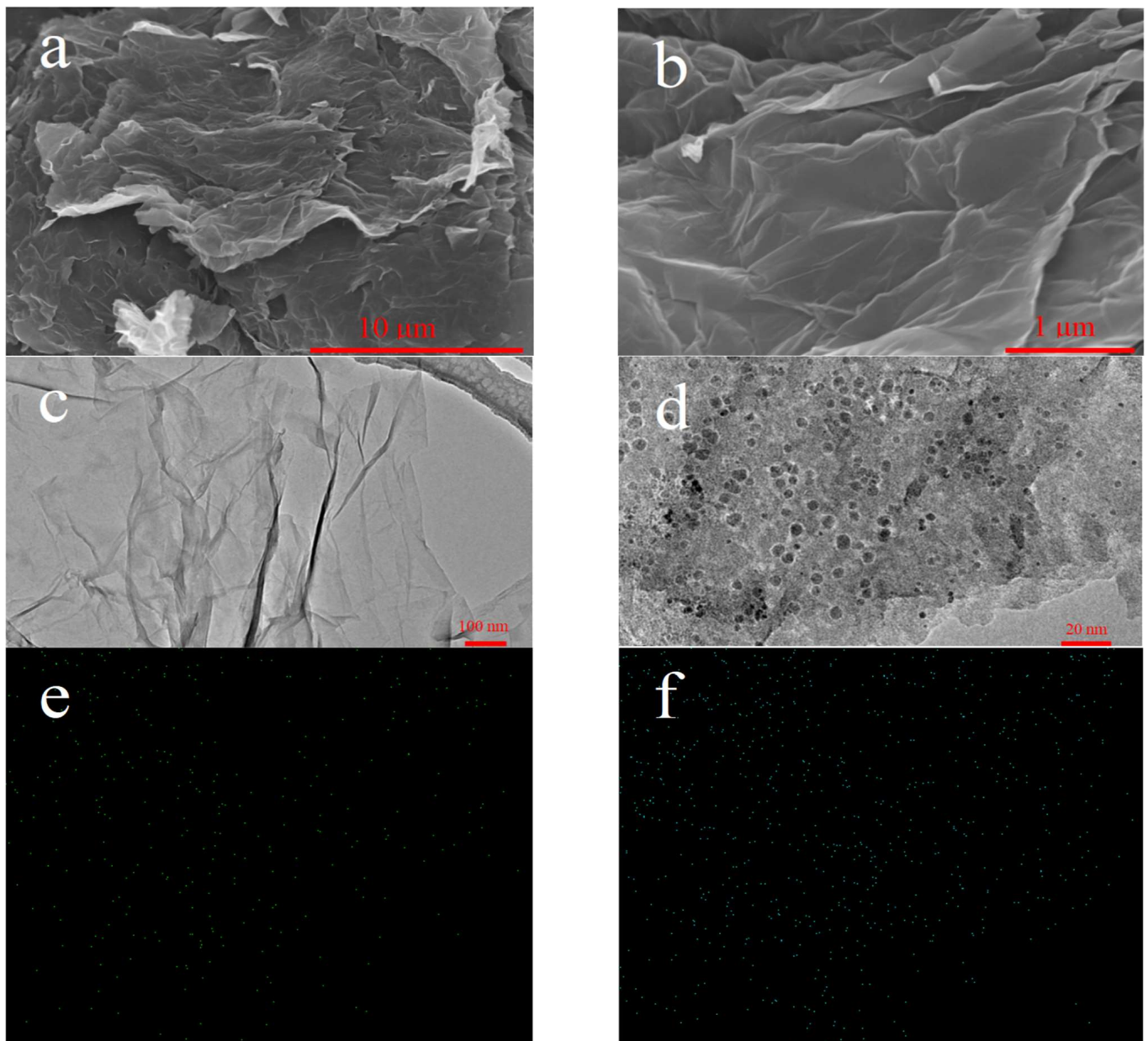

Figure 2. (**a**,**b**) SEM micrographs of the PtNi/S-(N)rGO; (**c**) HRTEM images of graphene oxide and (**d**) PtNi/S-(N)rGO; Mapping of (**d**) with different elements of (**e**)-N element and (**f**)-S elements.

The Raman spectrum was useful to evaluate the structure defects and doping amount of graphene materials [33]. The peaks of D band (1350 cm^{-1}), G band (1583.9 cm^{-1}), and 2D (2680 cm^{-1}) appeared in the graphene. D band was associated with disordered sp^2 carbon atoms, impurity atoms, defects, or phonon. G band was involved into the vibration of sp^2 carbon atom or the first order scattering of E$_{2g}$ mode. The peak of 2950 cm^{-1} reflected

a D+G combination mode, which was caused by defects. The intensity ratio of D and G band was depicted as the heteroatom doping and disordering of carbon structure in graphene [34]. The normalized Raman spectra of three samples are shown in Figure 3. The two featured peaks were shown in the Raman spectra. The ratio of I_D and I_G is 1.01, 1.10, and 1.13 for PtNi/rGO, PtNi/S-rGO, and PtNi/S-(N)rGO, respectively. The higher value was related with the high amount of doping and defects, which was in favor of the diffusion and adsorption of oxygen. The I_D/I_G of PtNi/S-(N)rGO was higher than that of other two catalysts, implying the more defect and N doping, lower graphitization, and disordering structure by the successful doping of N and S elements in sulfonated groups. The sulfonated groups could separate the graphene nano-sheets, which also caused a more disorder structure and high value of I_D/I_G.
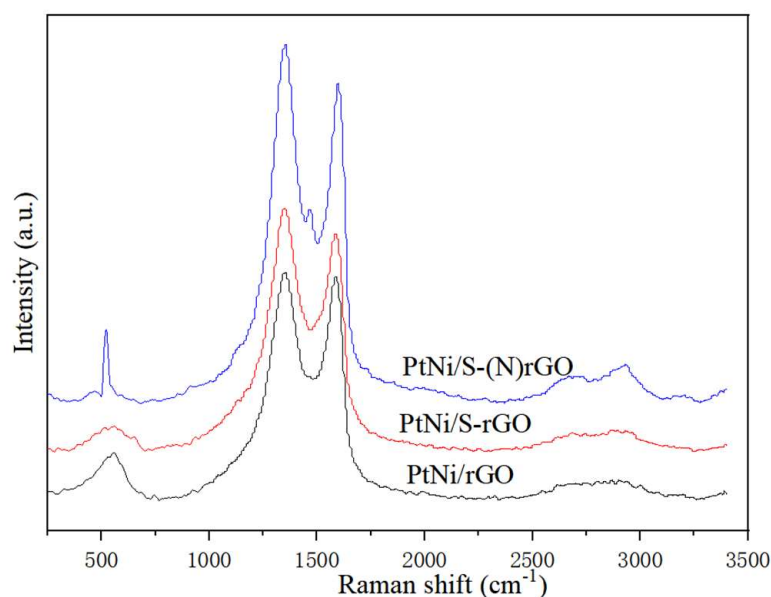

Figure 3. The normalized Raman spectra of PtNi/S−(N)rGO, PtNi/S−rGO, and PtNi/rGO.

The surface properties of PtNi/rGO, PtNi/S-rGO, and PtNi/S-(N)rGO were characterized by the zeta potential analyzer. It was shown that the zeta surface potential of PtNi/rGO was 4.5 ± 1 mV, which demonstrated the reduction of GO by eliminating the epoxy and hydroxyl groups on the C atom of graphene. The value of potential of PtNi/S-rGO and PtNi/S-(N)rGO shifted to the -50 ± 2 and -55 ± 2 mV, respectively. The surface properties of catalyst were changed by formation of the sulfonated groups instead of the protons of rGO.

XPS measurements were used to identify the bonds of different elements (N, S, Pt, Ni, C) in the PtNi/(N)S-rGO catalyst, which was confirmed by the EDS analysis. The high-resolution spectra of XPS for the PtNi/(N)S-rGo catalyst was shown in Figure 4. The two peaks were corresponded to the Pt 4f 7/2 and Pt 4f 5/2 spectrum at 71.20 and 74.55 eV for deconvoluted Pt, respectively. Substantial Pt^{2+} states (72.4 and 75.7 eV) were observed in the catalyst. There were no Pt^{4+} states in the nanoparticles. The other metal element of Ni (853.2 and 869.9 eV) was deconvoluted to 2p spectrum in Figure 4b. The parts of Ni were oxidated by the hydroxylation as shown in the Ni^{2+} spectra (858.0 and 876.4 eV). There were three typical states of N doping in graphene: pyridinic (ca.398 eV), amino (ca.399.05 eV), and pyrrolic (ca.399.63 eV) in Figure 4c. The detailed structures of pyridinic and pyrrolic were discussed in reference [35]. The C 1s spectrum was assigned to the C-C/C=C (284.5 eV), C-N (285.5 eV), C-O (287.9 eV), C-S (292.5 eV), and C=O (295.2 eV). The S 2p region of PtNi/S-(N)rGO was deconvoluted to one peak, which presented the formation of $-SO_3H$ group on the reduced graphene oxide around 166.9 eV. The existence of S and N elements were also confirmed by the mapping of elements in Figure 2e,f.
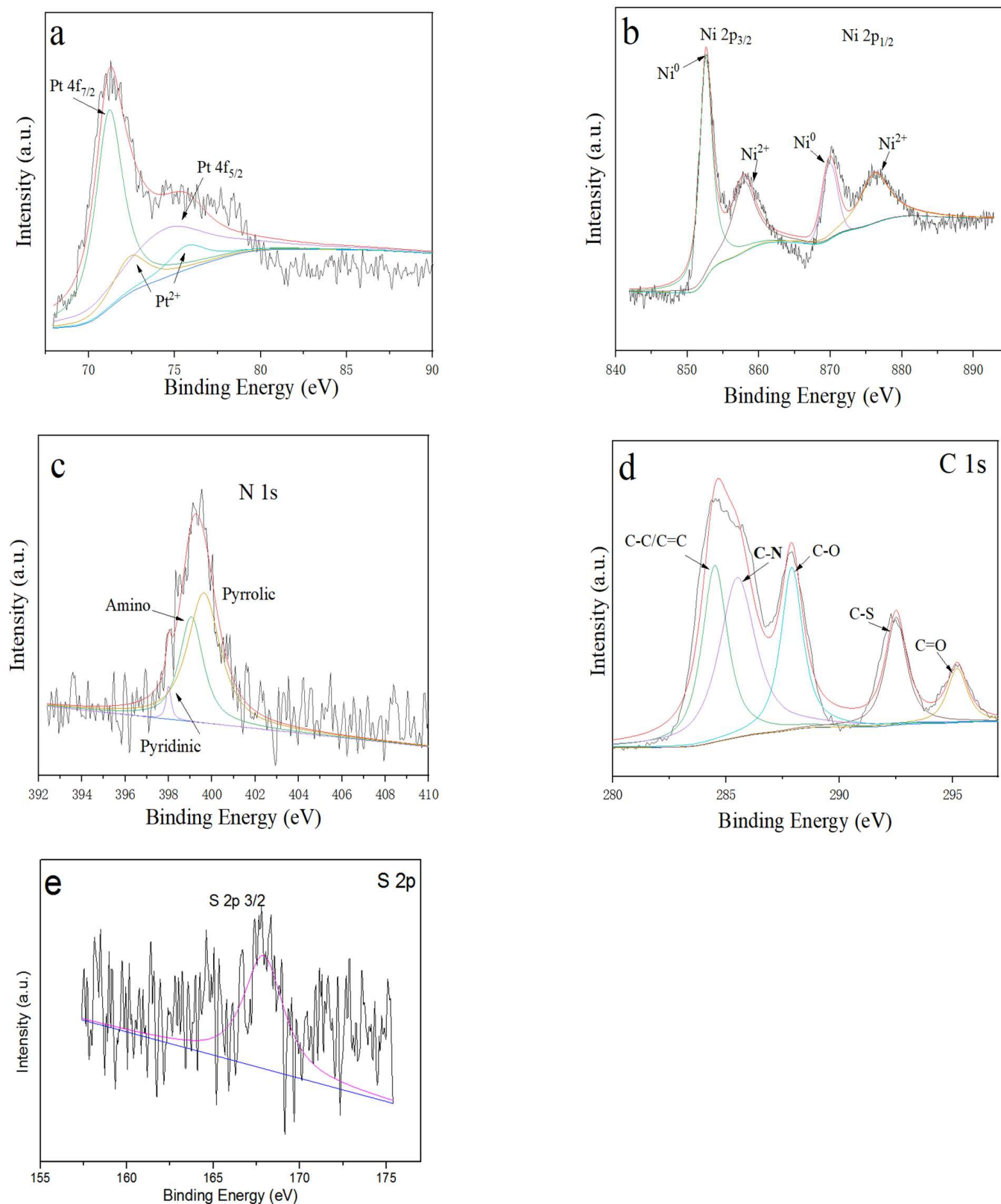
Figure 4. XPS spectra for different elements of PtNi/(N)S-rGo catalyst (**a**) Pt (**b**) Ni (**c**) N (**d**) C (**e**) S.

Figure 5a showed the N_2-adsorpion/desorption isotherms of supporting materials without the PtNi nanoparticles. The surface areas of BET of rGO, S-rGO, and S-(N)rGO were 180.7, 277.8, and 295.3 m^2/g, respectively. It was shown that the S-rGO was in favor of reducing the agglomeration of graphene. The N-doped could provide more activated

sites for anchoring the -SO₃H group. Therefore, the supporting materials of the S-(N)rGO exhibited the maximum value of BET surface area. Figure 5b showed the image of pore size distribution of supporting materials. The mesopores existed in the three supporting materials with 2–10 nm in widths. There was no obvious change of pore distribution among rGO, S-rGO, and S-(N)rGO supporting materials. It was demonstrated that there was no significant effect of N doping and S-rGO groups on the pore size and distribution.
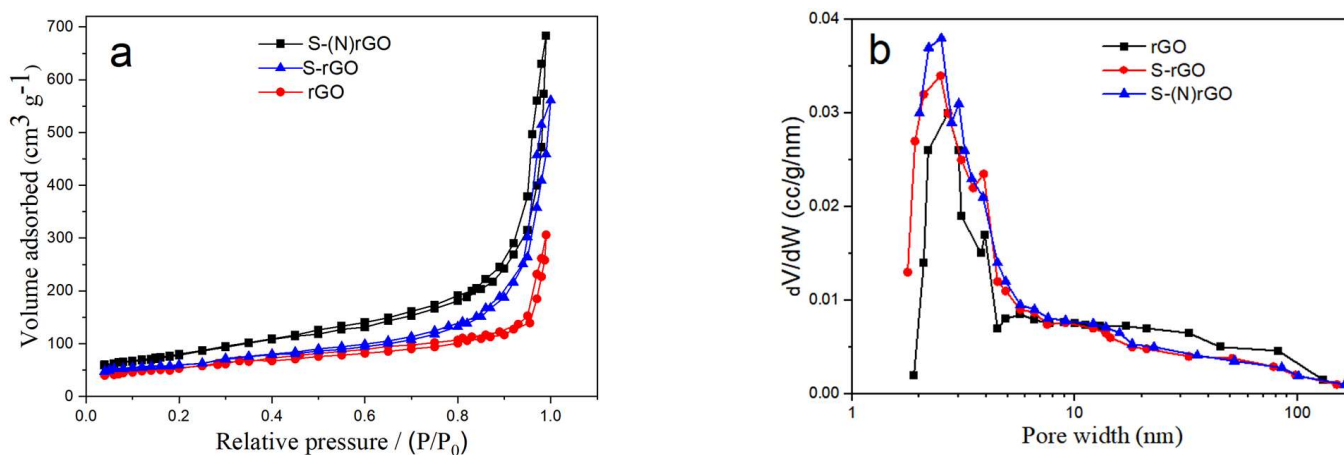

Figure 5. (**a**) N₂ adsorption/desorption isotherms of the supporting materials at 77 K; (**b**) Pore size distribution of the supporting materials calculated by the Barrett−Joyner−Halenda formula from the desorption branch of N₂ adsorption.

The steady-state current for ORR polarization curves of the Pt/C, PtNi/S-rGO, and PtNi/S-(N)rGO catalysts were measured in the 0.5 M H₂SO₄ electrolytes in Figure 6a. It was revealed that the values of limited current for the Pt/C, PtNi/S-rGO, and PtNi/S-(N)rGO catalysts were 4.01, 5.1, and 5.99 mA/cm² at rotating disk electrode of 800 rpm, respectively. Accordingly, the half-wave potentials of the Pt/C, PtNi/S-rGO, and PtNi/S-(N)rGO catalysts were 0.596, 0.627, and 0.632 V, respectively. There was a positive shift of half-wave potential among the three catalysts. It was indicated that the catalytic activity of the PtNi/S-(N)rGO catalyst was superior to the other two catalysts. In order to investigate the kinetics of ORR of the PtNi/S-(N)rGO catalyst, the polarization curves were measured by the rotating disk electrode (RDE). The limited current density was related with the speed of the RDE. Figure 6b shows the limiting currents at the different rates of rotating. The current density increased with the increase of rotating rate by the concentration gradient of diffusion on the surface of electrode. A Koutechy–Levich equation was used to calculate the number of electron transfer in the ORR of the PtNi/S-(N)rGO catalyst as follows [36]:

$$\frac{1}{I} = \frac{1}{I_k} + \frac{1}{B\omega^{0.5}} \tag{2}$$

where I was the overall ORR current density from the experimental results of the polarization curves of ORR, I_k was the kinetic current, and ω was the rotation rate of disk electrode. The parameter B was calculated by the following equation:

$$B = 0.62nFC_{O_2} \left(D_{O_2}\right)^{2/3} v^{-1/6} \tag{3}$$

where n represented the number of electron transfer, F was the Faraday constant (96,486 C/mol), C_{O_2} was the concentration of saturated oxygen in 0.5 M H₂SO₄ aqueous solution (1.13×10^{-3} mol/L), D_{O_2} was the diffusion coefficient of oxygen in solution (1.8×10^{-5} cm² s⁻¹), and v was the viscosity of solution (1×10^{-2} cm² s⁻¹). The three limited currents were fitted into a linear regression parameter ($R^2 = 0.994$). The fitted results of high quality showed that the model was useful to validate the kinetic parameter. The linearity appearing in Figure 6b was effectively proved to be the first

order of reduction reaction of dissolved oxygen in solution. From the calculation of Equations (2) and (3), the number of electron transfer was 3.84 at 0.2 V, 3.9 at 0.4 V, and 3.78 at 0.6 V. Sulfonated groups could facilitate stable adsorption of OOH* intermediates on Pt surface, which broke the O-O bond easily. N-doped graphene could reduce the energy barrier for improving the rate-determining steps of sluggish kinetics. The reaction of OH* intermediate was excluded by high catalytic activity. The protonation of OOH* to produce H_2O_2 was suppressed by the PtNi/S-(N)rGO catalyst [37]. The most reactions were decided by almost four electrons rout. It was shown that the excellent activity of catalyst for introducing N-doping and sulfonation on graphene supports.
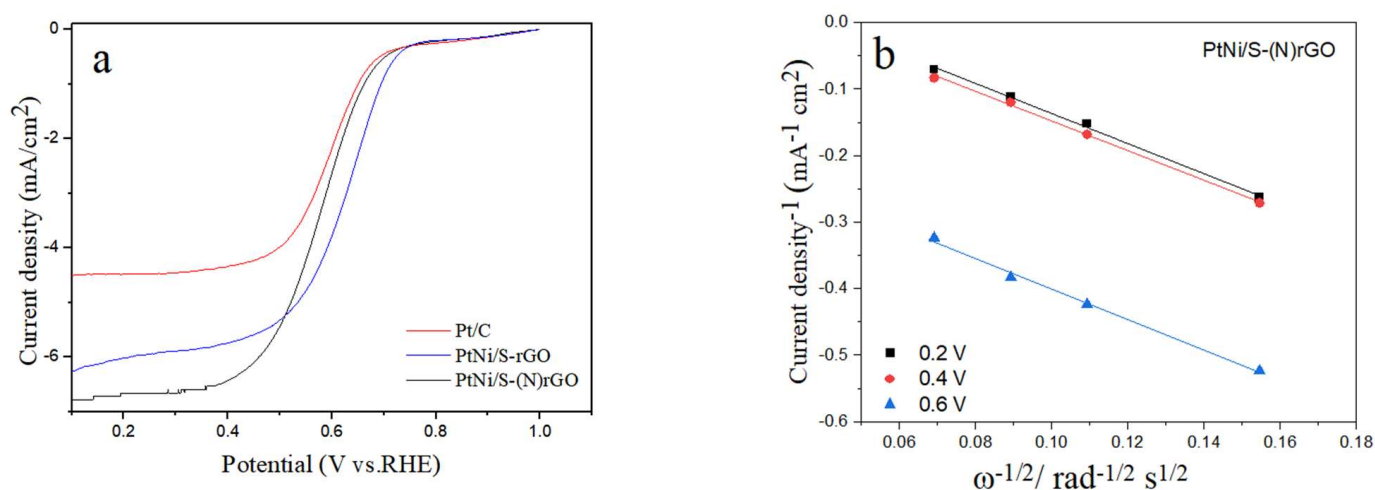

Figure 6. In the Pt/C, PtNiCo/S−rGO, and PtNiCo/S−(N)rGO catalysts (**a**) CV curves for redox reaction (**b**)Limited current for ORR.

The electrochemical acceleration tests were used to characterize the durability of catalysts of ORR in Figure 7. Obviously, the durability of the Pt/C catalyst was much lower than that of PtNi/S-rGO and PtNi/S-(N)rGO. At the initial stage, the decrease of ECSA for Pt/C was larger than that of the PtNi/S-rGO and PtNi/S-(N)rGO catalysts. After 5000 cycles, the ECSA of the sample remained 60.2% of initial value for PtNi/S-(N)rGO, 50.5% of initial value for PtNi/S-rGO, and 19.5% of initial value for Pt/C, respectively. The durability of PtNi/S-rGO was 2.6 time higher than of the Pt/C catalyst and the durability PtNi/S-(N)rGO was 3.1 times higher than that of the Pt/C catalyst. It was indicated that the sulfonation groups were good at anchoring the PtNi nanoparticles. Thus, the durability of PtNi/S-(N)rGO for ORR was greatly improved by the stability of PtNi nanoparticles on the sulfonation groups.

Figure 8 shows the polarization and power density of PtNi/S-(N)rGO and commercial Pt/C as the cathode, with commercial Pt/C as the anode for testing in single fuel cell. The polarization curves of PEMFC were divided into three parts corresponding to three stages of polarization, which were electrochemical, ohmic, and concentration polarization, respectively. The key stages were 81 mA cm^{-2} at 0.77 V and 792 mA cm^{-2} at 0.34 V for the commercial Pt/C catalyst. However, the key stages were 162 mA cm^{-2} at 0.75 V and 962 mA cm^{-2} at 0.39 V for the PtNi/S-(N)rGO catalyst. The peak power density of the commercial Pt/C and PtNi/S-(N)rGO catalysts were 0.64 W cm^{-2} at 640 mA cm^{-2} and 0.88 W cm^{-2} at 387 mA cm^{-2}, respectively. The power density of the prepared catalyst was improved 37.5% higher compared to the commercial Pt/C catalyst.
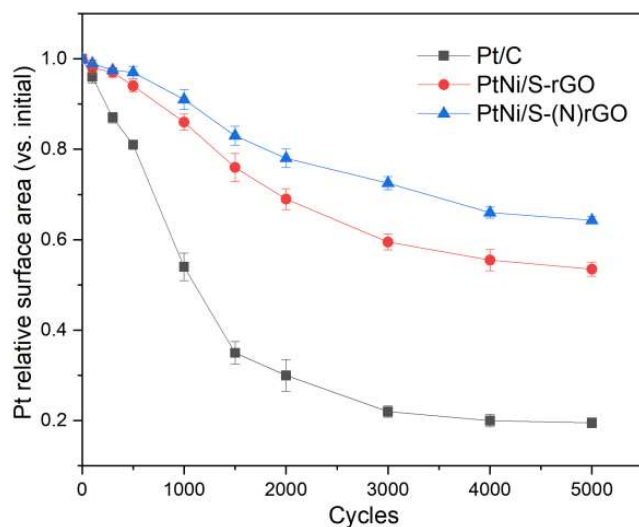
Figure 7. Changes of ECSA of three catalysts with different cycles under the same electrochemical acceleration test.
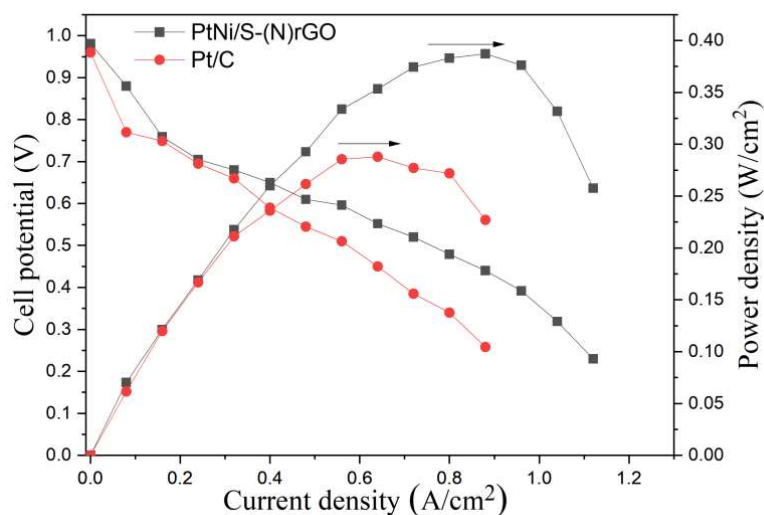

Figure 8. Polarization and power density curves for membrane electrode assembly with PtNi/S-(N)rGO and Pt/C catalysts as the cathode of single cell.

In the initial polarization stage, the Pt/C catalyst had larger drop in potential and more different chemical reaction than that of the PtNi/S-(N)rGO catalyst. The result was attributed to the easy wettability of the PtNi/S-(N)rGO catalyst in solution by the sulfonated groups. Then oxygen could be reduced easily by the Pt nanoparticles anchored on the sulfonated groups. In the second stage, the ohmic polarizations were smaller than that of the commercial Pt/C catalyst. The sulfonated groups were in favor of the evenly distribution of PtNi nanoparticles on the supports. Then, the PtNi/S-(N)rGO catalyst showed the excellent conductivity. At the same time, the higher power density of PtNi appeared at the stage of concentration polarization in the process of ORR. Therefore, the property of PEMFC with the PtNi/S-(N)rGO catalyst as the cathode was better than that of the commercial Pt/C catalyst.

4. Conclusions

In summary, PtNi nanoparticles were decorated on N-doped and sulfonated reduced graphene oxide by simple thermal decomposition and hydrothermal treatment. The PtNi nanoparticles were anchored at the sulfonated groups on N-doped graphene sheets evenly and strongly, which resulted in higher half-wave potential. The PtNi/S-(N)rGO showed

stable and effective catalytic properties for ORR in proton exchange membrane fuel cell. The good properties of electrocatalysis were also attributed to the excellent affinity of N atom and sulfonated groups to reactive species from oxygen molecular and hydrogen ions. The MEAs made with the PtNi/S-(N)rGO catalyst provided higher power density and current density superior to that of the commercial Pt/C catalyst. Therefore, the commercially available PtNi/S-(N)rGO catalyst can be used in the cathode of PEMFCs in the future.

References

1. López-Chávez, E.; Garcia-Quiroz, A.; Jiménez-González, L.J.; Díaz-Góngora, J.A.I.; Peña-Castañeda, Y.A. Quantum chemistry of the oxygen reduction reaction (ORR) on Fe-G iron doped graphene for fuel cells. *Int. J. Hydrog. Energy* **2019**, *44*, 12439–12445. [CrossRef]
2. Chen, J.; Ou, Z.; Chen, H.; Song, S.; Wang, K.; Wang, Y. Recent developments of nanocarbon based supports for PEMFCs electro-catalysts. *Chin. J. Catal.* **2021**, *42*, 1297–1326. [CrossRef]
3. Okonkwo, P.C.; Ige, O.O.; Barhoumi, E.M.; Uzoma, P.C.; Emori, W.; Benamor, A.; Abdullah, A.M. Platinum degradation mechanisms in proton exchange membrane fuel cell (PEMFC) system: A review. *Int. J. Hydrog. Energy* **2021**, *46*, 15850–15865. [CrossRef]
4. Wang, Y.; Han, C.; Xie, P.; Li, H.; Yao, P.; Cao, J.; Ruan, M.; Song, P.; Gong, X.; Lu, M.; et al. Highly dispersed PtNi nanoparticles modified carbon black as high-performanced electrocatalyst for oxygen reduction in acidic medium. *J. Electroanal. Chem.* **2022**, *904*, 115908. [CrossRef]
5. Cheng, X.; Wang, Y.; Lu, Y.; Zheng, L.; Sun, S.; Li, H.; Chen, G.; Zhang, J. Single-atom alloy with Pt-Co dual sites as an efficient electrocatalyst for oxygen reduction reaction. *Appl. Catal. B Environ.* **2022**, *306*, 121112. [CrossRef]
6. Fortunato, G.V.; Cardoso, E.S.F.; Martini, B.K.; Maia, G. Ti/Pt−Pd-Based Nanocomposite: Effects of Metal Oxides on the Oxygen Reduction Reaction. *ChemElectroChem* **2020**, *7*, 1610–1618. [CrossRef]
7. Luo, M.; Qin, Y.; Li, M.; Sun, Y.; Li, C.; Li, Y.; Yang, Y.; Lv, F.; Wu, D.; Zhou, P.; et al. Interface modulation of twinned PtFe nanoplates branched 3D architecture for oxygen reduction catalysis. *Sci. Bull.* **2020**, *65*, 97–104. [CrossRef]
8. Guerra-Balcázar, M.; Cuevas-Muñiz, F.M.; Álvarez-Contreras, L.; Arriaga, L.G.; Ledesma-García, J. Evaluation of bimetallic catalyst PtAg/C as a glucose-tolerant oxygen reduction cathode. *J. Power Sources* **2012**, *197*, 121–124. [CrossRef]
9. Liu, Y.; Du, L.; Kong, F.; Han, G.; Gao, Y.; Du, C.; Zuo, P.; Yin, G. Sulfur Dioxide-Tolerant Bimetallic PtRu Catalyst toward Oxygen Electroreduc-tion. *ACS Sustain. Chem. Eng.* **2020**, *8*, 1295–1301. [CrossRef]
10. Chung, S.; Ham, K.; Kang, S.; Ju, S.; Lee, J. Enhanced corrosion tolerance and highly durable ORR activity by low Pt electrocatalyst on unique pore structured CNF in PEM fuel cell. *Electrochim. Acta* **2020**, *348*, 136346. [CrossRef]
11. Li, W.; Zou, S. PtNi Nanoparticles Encapsulated in Few Carbon Layers as High-Performance Catalysts for Oxygen Reduction Reaction. *ACS Appl. Energy Mater.* **2019**, *2*, 2769–2778. [CrossRef]
12. Cao, L.; Zhao, Z.; Liu, Z.; Gao, W.; Dai, S.; Gha, J.; Xue, W.; Sun, H.; Duan, X.; Pan, X.; et al. Differential Surface Elemental Distribution Leads to Significantly Enhanced Stability of PtNi-Based ORR Catalysts. *Matter* **2019**, *1*, 1567–1580. [CrossRef]
13. Zhao, Y.; Tao, L.; Dang, W.; Wang, L.; Xia, M.; Wang, B.; Liu, M.; Gao, F.; Zhang, J.; Zhao, Y. High-Indexed PtNi Alloy Skin Spiraled on Pd Nanowires for Highly Efficient Oxygen Reduction Reaction Catalysis. *Small* **2019**, *15*, 1900288. [CrossRef] [PubMed]
14. Martins, M.; Milikić, J.; Šljukić, B.; Soylu, G.S.P.; Yurtcan, A.B.; Bozkurt, G.; Santos, D.M.F. Mn2O3-MO (MO = ZrO2, V2O5, WO3) supported PtNi nanoparticles: Designing stable and efficient electrocatalysts for oxygen reduction and borohydride oxidation. *Mi-Croporous Mesoporous Mater.* **2019**, *273*, 286–293. [CrossRef]
15. Zhang, W.; Xiao, Y. Mechanism of Electrocatalytically Active Precious Metal (Ni, Pd, Pt, and Ru) Complexes in the Graphene Basal Plane for ORR Applications in Novel Fuel Cells. *Energy Fuels* **2020**, *34*, 2425–2434. [CrossRef]
16. Reda, M.; Hansen, H.A.; Vegge, T. DFT study of stabilization effects on N-doped graphene for ORR catalysis. *Catal. Today* **2018**, *312*, 118–125. [CrossRef]

17. Yan, P.; Liu, J.; Yuan, S.; Liu, Y.; Cen, W.; Chen, Y. The promotion effects of graphitic and pyridinic N combinational doping on gra-phene for ORR. *Appl. Surf. Sci.* **2018**, *445*, 398–403. [CrossRef]

18. Balaji, S.S.; Ganesh, P.A.; Moorthy, M.; Sathish, M. Efficient electrocatalytic activity for oxygen reduction reaction by phospho-rus-doped graphene using supercritical fluid processing. *Bull. Mater. Sci.* **2020**, *43*, 151. [CrossRef]

19. Li, R.; Wei, Z.; Gou, X.; Xu, W. Phosphorus-doped graphene nanosheets as efficient metal-free oxygen reduction electrocata-lysts. *RSC Adv.* **2013**, *3*, 9978–9984. [CrossRef]

20. Zhang, C.; Mahmood, N.; Yin, H.; Liu, F.; Hou, Y. Synthesis of Phosphorus-Doped Graphene and its Multifunctional Applications for Oxygen Reduction Reaction and Lithium Ion Batteries. *Adv. Mater.* **2013**, *25*, 4932–4937. [CrossRef]

21. Jang, D.; Lee, S.; Kim, S.; Choi, K.; Park, S.; Oh, J.; Park, S. Production of P, N Co-doped Graphene-Based Materials by a Solution Pro-cess and Their Electrocatalytic Performance for Oxygen Reduction Reaction. *ChemNanoMat* **2018**, *4*, 118–123. [CrossRef]

22. Zhang, J.; Dai, L. Nitrogen, Phosphorus, and Fluorine Tri-doped Graphene as a Multifunctional Catalyst for Self-Powered Electrochemical Water Splitting. *Angew. Chem. Int. Ed.* **2016**, *128*, 13490–13494. [CrossRef]

23. Kim, H.; Yang, H.; Kang, J.; Takeuchi, N. Multifunctional Disordered Sulfur-Doped Carbon for Efficient Sodium-Ion-Exchange and 2-Electron-Transfer-Dominant Oxygen Reduction Reaction. *Carbon* **2021**, *182*, 242–253. [CrossRef]

24. Bouleau, L.; Pérez-Rodríguez, S.; Quílez-Bermejo, J.; Izquierdo, M.; Xu, F.; Fierro, V.; Celzard, A. Best practices for ORR performance evaluation of metal-free porous carbon electrocatalysts. *Carbon* **2022**, *189*, 349–361. [CrossRef]

25. Banerjee, P.; Das, G.P.; Thapa, R. Computationally exploring the role of S-dopant and S-linker in activating the catalytic effi-ciency of graphene quantum dot for ORR. *Catal. Today* **2021**, *370*, 36–45. [CrossRef]

26. Lu, L.; Zheng, Y.; Yang, R.; Kakimov, A.; Li, X. Recent advances of layered double hydroxides–based bifunctional electrocatalysts for ORR and OER. *Mater. Today Chem.* **2021**, *21*, 100488. [CrossRef]

27. Hung, T.-F.; Wang, B.; Tsai, C.-W.; Tu, M.-H.; Wang, G.-X.; Liu, R.-S.; Tsai, D.P.; Lo, M.-Y.; Shy, D.-S.; Xing, X.-K. Sulfonation of graphene nanosheet-supported platinum via a simple thermal-treatment toward its oxygen reduction activity in acid medium. *Int. J. Hydrog. Energy* **2012**, *37*, 14205–14210. [CrossRef]

28. Mena-Durán, C.J.; Alonso-Lemus, I.L.; Quintana, P.; Barbosa, R.; Ordoñez, L.C.; Escobar, B. Preparation of metal-free electrocata-lysts from cassava residues for the oxygen reduction reaction: A sulfur functionalization approach. *Int. J. Hydrog. Energy* **2018**, *43*, 3172–3179. [CrossRef]

29. Carrillo-Rodríguez, J.; Garay-Tapia, A.; Escobar-Morales, B.; Escorcia-García, J.; Ochoa-Lara, M.; Rodríguez-Varela, F.; Alonso-Lemus, I. Insight into the performance stability of N-doped Ordered Mesoporous Carbon Hollow Spheres for the ORR: Influence of the nitrogen species on their catalytic activity after, A.D.T. *Int. J. Hydrog. Energy* **2021**, *46*, 26087–26100. [CrossRef]

30. Han, G.; Li, L.; Li, X.; Sun, Y.; Du, C.; Gao, Y.; Yin, G. Proof-of-concept fabrication of carbon structure in Cu–N–C catalysts of both high ORR activity and stability. *Carbon* **2021**, *174*, 683–692. [CrossRef]

31. Wang, G.; Yang, Z.; Du, Y.; Yang, Y. Programmable Exposure of Pt Active Facets for Efficient Oxygen Reduction. *Angew. Chem. Int. Ed.* **2019**, *58*, 15848–15854. [CrossRef] [PubMed]

32. Intan, N.N.; Pfaendtner, J. Composition of Oxygen Functional Groups on Graphite Surfaces. *J. Phys. Chemis-Try C* **2022**, *126*, 10653–10667. [CrossRef]

33. Chakrabarty, S.; Mukherjee, A.; Su, W.-N.; Basu, S. Improved bi-functional ORR and OER catalytic activity of reduced graphene oxide supported $ZnCo_2O_4$ microsphere. *Int. J. Hydrog. Energy* **2019**, *44*, 1565–1578. [CrossRef]

34. Lee, S.J.; Theerthagiri, J.; Nithyadharseni, P.; Arunachalam, P.; Balaji, D.; Madan Kumar, A.; Madhavan, J.; Mittal, V.; Choi, M.Y. Heteroatom-doped gra-phene-based materials for sustainable energy applications: A review. *Renew. Sustain. Energy Rev.* **2021**, *143*, 110849. [CrossRef]

35. Saravanan, K.; Gottlieb, E.; Keith, J.A. Nitrogen-doped nanocarbon materials under electroreduction operating conditions and implications for electrocatalysis of CO_2. *Carbon* **2017**, *111*, 859–866. [CrossRef]

36. Akula, S.; Mooste, M.; Zulevi, B.; McKinney, S.; Kikas, A.; Piirsoo, H.-M.; Rähn, M.; Tamm, A.; Kisand, V.; Serov, A.; et al. Mesoporous textured Fe-N-C electrocatalysts as highly efficient cathodes for proton exchange membrane fuel cells. *J. Power Sources* **2022**, *520*, 230819. [CrossRef]

37. Lee, J.; Kumar, A.; Yang, T.; Liu, X.; Jadhav, A.R.; Park, G.H.; Hwang, Y.; Yu, J.; Nguyen, C.T.K.; Liu, Y.; et al. Stabilizing the OOH * intermediate via pre-adsorbed surface oxy-gen of a single Ru atom-bimetallic alloy for ultralow overpotential oxygen generation. *Energy Environ. Sci.* **2020**, *13*, 5152–5164. [CrossRef]